Lawrence Berkeley National Laboratory

Title
Topology-dependent stability of vortex-antivortex structures

Authors
Han, Hee-Sung
Lee, Sooseok
Jung, Min-Seung
et al.

Topology-dependent stability of vortex-antivortex structures

Hee-Sung Han[1,2], Sooseok Lee[2], Min-Seung Jung[3], Namkyu Kim[2], Weilun Chao[1], Young-Sang Yu[4], Jung-Il Hong[3], and Ki-Suk Lee[2*], Mi-Young Im[1*]

AFFILIATIONS

[1]Center for X-ray Optics, Lawrence Berkeley National Laboratory, Berkeley, CA, 94720, USA

[2]School of Materials Science and Engineering, Ulsan National Institute of Science and Technology (UNIST), Ulsan, 44919, Republic of Korea

[3]Department of Emerging Materials Science, DGIST, Daegu 42988, Republic of Korea

[4]Advanced Light Source, Lawrence Berkeley National Laboratory, Berkeley, CA, 94720, USA

*Correspondence and requests for materials should be addressed to K.-S. L. (email: kisuk@unist.ac.kr) or to M.-Y. I (email: mim@lbl.gov).

1 **ABSTRACT**

2   The non-trivial topology of magnetic structures such as vortices and skyrmions is

3 considered as a key concept to explain the stability of those structures. The stability, dictated

4 by non-trivial topology, provides great potential for device applications. Although it is a very

5 critical scientific and technological issue, it is elusive to experimentally study the topology-

6 dependent stability owing to the difficulties in establishing stably formed magnetic structures

7 with different topologies. Here, we establish a platform for vortex-antivortex structures with

8 different topological charges within $Ni_{80}Fe_{20}$ rectangular elements thick enough to stabilize a

9 unique three-dimensional magnetic structure with non-uniform magnetization along the

10 thickness of the elements. The detailed magnetization configurations of the three-dimensional

11 vortex-antivortex structures and their annihilations during their field-driven motions are

12 investigated by utilizing magnetic transmission soft x-ray microscopy and micromagnetic

13 simulation. We demonstrate that the stability of vortex-antivortex structures significantly

14 depends on their topologies and the topology-dependent stability is associated with their

15 different annihilation mechanisms. We believe that this work provides in-depth insight into

16 the stability of magnetic structures and its topology dependence.

17

18

1　　　　The localized swirling magnetic structures such as skyrmions, vortices, and

2　antivortices show scientifically and technologically intriguing physical behavior, which can

3　be understood by the concept of topology.[1-5] The topology of magnetic structures is

4　characterized by topological charge $q = \frac{1}{4\pi} \int \mathbf{m} \cdot \left(\frac{\partial \mathbf{m}}{\partial x} \times \frac{\partial \mathbf{m}}{\partial y} \right) dxdy$ where $\mathbf{m}$ is the normalized

5　magnetization vector.[1,6] The topologically non-trivial magnetic structures with $q \neq 0$ have

6　been thought to be more stable than those of topologically trivial magnetic structures with $q =$

7　0, which is closely associated with topologically protected properties of such magnetic

8　structures.[7,8] Indeed, it was experimentally demonstrated that skyrmions, which are

9　characterized by $q = +1$, show a longer lifetime than the topologically trivial bubble domains

10　with $q = 0$.[7] The stability of magnetic structures, dictated by topology, is a critical scientific

11　issue and also highly relevant to technological applications of magnetic structures to

12　nanodevices.

13　　　　In patterned soft magnetic materials, magnetic vortex and antivortex are

14　representative topologically non-trivial magnetic structures,[4,9-16] which provide a unique

15　playground for fundamental study on non-trivial nano-spin behavior. They are composed of

16　in-plane swirling magnetic components and out-of-plane (OOP) cores. The in-plane swirling

17　magnetic components are defined by the winding number n. Magnetic vortex and antivortex

1   are characterized by $n = +1$ and -1, respectively.[17-19] The direction of OOP cores is defined by

2   the polarity p. $p = +1$ and $p = -1$ represent upward and downward vortex cores, respectively.

3   Topologically, magnetic vortex and antivortex on the top (bottom) surface of a magnetic

4   element are characterized by $q = np/2$ $(-np/2) = +1/2$ $(-1/2)$ or $-1/2$ $(+1/2)$ depending on the

5   p of vortex and antivortex cores.[20,21] The vortex and antivortex can coexist in a patterned

6   ferromagnetic element and a vortex-antivortex (V-AV) structure can be stabilized in the

7   element.[22-25] The V-AV structure offers great potential for the applications of logic and

8   memory devices based on its topological properties.[24,25]

9   So far, the study on stability associated with the topology of magnetic structures has

10   been mainly focused on skyrmions.[7,8,26-28] On the other hand, the stability of V-AV structures

11   dictated by topology has been rarely addressed experimentally since it is difficult to stably

12   form topologically different V-AV structures. Moreover, the characterization of relevant

13   physical   behaviors   was   also   restricted   due   to   the   limited   availability   of

14   imaging/characterization tools.

15   In this work, we establish two stably formed topologically different V-AV structures

16   within 100 nm thick-$Ni_{80}Fe_{20}$ rectangular-patterned elements, where compelling three-

17   dimensional magnetic structures with non-uniform magnetization along the thickness of the

18   elements are created. We find that two V-AV structures are formed within three-dimensional

19   (3D) domain walls non-uniform along the thickness direction, and study field-driven behavior

1   of those two structures to investigate their stability by utilizing magnetic transmission soft X-

2   ray microscopy (MTXM) and micromagnetic simulations[29-31]. The topologically different V-

3   AV structures show distinct physical behavior from each other during their field-driven

4   motions. Our results demonstrate that the stability of V-AV structures depends on the

5   topology and the topology-dependent stability is deeply related to the annihilation mechanism

6   of V-AV structures.

7   Figure 1(a) illustrates the schematic diagram for X-ray imaging of a $Ni_{80}Fe_{20}$

8   rectangular element deposited on the Si_3N_4 membrane utilizing the MTXM (supplementary

9   material: A). To form various magnetic structures at the remanence, we repeated the

10   measurements of saturating the rectangular elements by applying the magnetic field of $H_x =$

11   100 mT in the x-axis and releasing them to zero field. Figures 1(b)-1(d) show MTXM images

12   of three different OOP magnetic structures observed within various $Ni_{80}Fe_{20}$ rectangular

13   elements with the thickness of $t = 100$ nm. The black and white contrasts represent upward

14   and downward OOP magnetic components, respectively. The lateral dimensions of the

15   elements in Figs. 1(b)-1(d) are 3×2 μm^2, 4.5×3 μm^2, and 4×2 μm^2, respectively. The

16   MTXM image in Fig. 1(b) shows a straight domain wall shown in black contrast indicating

17   OOP magnetic components pointing up. One noticeable thing is that in $-y$-direction with

18   respect to the domain wall, downward magnetic components (white contrast) along the

19   domain wall are clearly visible. Unlike the straight domain walls in Fig. 1(b), the domain

5

1   walls in Figs. 1(c) and 1(d) are bent. More interestingly, the detailed magnetic configuration

2   around the kinked areas of the two domain walls is quite different from each other as shown

3   in the zoomed images. The upward polarization of the domain wall in Fig. 1(c) remains the

4   same even if it is slightly bent. However, the downward magnetic components, visible as a

5   white contrast in the image of Fig.1(b), no longer continues along the domain wall. On the

6   left side of the kinked area, the segment of downward magnetic components is positioned in

7    $-y$-direction with respect to the domain wall while it is located in $+y$-direction with respect to

8   the domain wall on the right side of the kinked area. The domain wall in Fig. 1(d) is more

9   complicated. The polarization of the domain wall switches from upward to downward at the

10   kink. The domain wall segments with upward and downward polarizations are paired with

11   downward and upward magnetic components, respectively, and both downward and upward

12   magnetic components are positioned in $+y$-direction with respect to the domain wall

13   segments.

14   For better understanding those observed magnetic structures and their internal

15   magnetic configurations, we reproduced images for magnetic structures by micromagnetic

16   simulations with consideration of magnetic grains to mimic realistic conditions of real

17   systems, where intrinsic defects inevitably exist (supplementary material: A). In Figs. 1(e)-

18   1(g), simulated magnetic images, which match well with the MTXM images, are displayed.

19   The zoomed images of magnetic structures indicated by red boxes are inserted in Figs. 1(c)-

1   1(d), and 1(f)-1(g) where domain walls with upward and downward polarizations are

2   represented by the red and blue dotted lines, respectively. Figures 1(h)-1(j) show 3D

3   magnetic configurations of the magnetic structures indicated by the yellow dashed boxes in

4   Figs.1(e)-1(g). The red and blue colors represent volumes with the normalized

5   magnetizations of $m_z \geq +0.8$ and $m_z \leq -0.8$, respectively. Therefore, the colored elongated

6   structures in Figs. 1(h)-1(j) correspond to the domain walls observed in MTXM

7   measurements (Figs. 1(b)-1(d)). The 3D images in Figs. 1(h)-1(j) clearly show the

8   magnetization is not uniform along the thickness direction. It presents that the domain walls

9   in the middle part of the rectangular element connect vortex and/or antivortex core on the top

10 and bottom surfaces of the rectangular elements. One interesting point is that the domain

11 walls consist of not only upward OOP Bloch components (hereafter called cores) in the

12 middle part of the rectangular element but also in-plane Néel components, called Néel caps

13 (hereafter called caps) on the top and bottom surfaces of the element[32-36] as indicated in the

14 cross-section images of Figs. 1(h)-1(j). In addition, OOP Bloch components of the domain

15 wall are paired with oppositely polarized OOP components (see small arrows in the cross-

16 section images) and the flux-closure domains are formed on the yz-plane of the element,

17 which likely reduces demagnetization energy. This result supports that the OOP magnetic

18 component observed in $-y$-direction or $+y$-direction with respect to the domain walls in

19 MTXM images (Figs. 1(b)-1(d)) is the other OOP component of the flux-closure domain

paired with the OOP Bloch component of the domain wall. Interestingly, the domain wall

composed of cap and core (hereafter called asymmetric Bloch wall, ABW) can be

transformed through the switching of cap and core within the ABW.[34,37] Images in Figs. 1(c)

and 1(d) show ABWs with a cap switch and with both cap and core switches, respectively.

Within the ABW in Fig. 1(i), at the point where cap switching occurs as indicated in cross-

section images, the vortex and antivortex with $p = +1$ are generated on the top and bottom

surfaces of the element, respectively. In the ABW in Fig. 1(j), the antivortex and vortex are

generated at the kink as seen in the ABW in Fig. 1(i). However, the vortex cores connected

by the ABW segment on the right side of the kink have $p = -1$ due to the core switch. The

cap and core switches along with the switching of rotational sense of flux-closure domains

are identified in MTXM images in Figs. 1(b)-1(d). The results in Figs. 1(i) and 1(j) show that

V-AV structures can be established through cap and core switches in the rectangular elements

where the magnetization is not uniform along the thickness direction. More interestingly, we

found that topological charges of V-AV structures ($q_{V\text{-}AV}$) indicated by green boxes in Figs.

1(i) and 1(j) are different. The $q_{V\text{-}AV}$ of V-AV structure (hereafter, called V-AV$_{q=0}$ structure) in

Fig. 1(i) is zero ($q_V = -1/2$ and $q_{AV} = +1/2$), which is topologically trivial, while the V-AV

structure (hereafter, called V-AV$_{q=-1}$ structure) in Fig. 1(j) is not topologically trivial as it is

characterized by $q_{V\text{-}AV} = -1$ ($q_V = -1/2$ and $q_{AV} = +1/2$) (supplementary material: B). That is,

those two V-AV structures stably established in $Ni_{80}Fe_{20}$ rectangular elements are

1   topologically different. The 3D magnetic elements, 100 nm-thick $Ni_{80}Fe_{20}$ rectangular

2   elements, can stabilize two topologically different V-AV structures.

3   We investigated the physical behavior of those topologically different V-AV

4   structures by applying external magnetic fields (Fig. 2). MTXM images in Fig. 2(a) show that

5   the vortex and the antivortex get close to each other with increasing the field from $H_y = 0$ mT

6   to $H_y = 10$ mT. At $H_y = 12$ mT, the antivortex generated by the cap switch disappears together

7   with the vortex, which is identified by the straight ABW that remains without the kink. The

8   simulation result in Fig. 2(b) also shows the annihilation of the V-AV$_{q=0}$ structure as observed

9   in MTXM images. The detailed annihilation process of the V-AV$_{q=0}$ structure is illustrated in

10   Fig. 2(c). On the bottom surface of the rectangular element, the vortex with $q_V = -1/2$ moves

11   toward the antivortex with $q_{AV} = +1/2$ as the magnetic field increases. Once the antivortex

12   with $q_{AV} = +1/2$ and the vortex with $q_V = -1/2$ on the bottom surface of the rectangular

13   element get close enough, the two merge and disappear. The annihilation of V-AV$_{q=0}$

14   structure is topologically trivial process. The annihilation can be considered as continuous

15   transformation of V-AV$_{q=0}$ structure into another topologically trivial magnetic structure with

16   $q = 0$ in the same homotopy class. There is no energy barrier associated with the topology to

17   overcome for the V-AV$_{q=0}$ structure to be annihilated. It explains why the V-AV$_{q=0}$ structure

18   can be easily annihilated.

19   To investigate the stability of topologically non-trivial V-AV structure, we

1   performed the same type of measurement for the V-AV$_{q=-1}$ structure as shown in Fig. 1(d).

2   The antivortex and the vortex get closer to each other with increasing the magnetic field as

3   observed in the V-AV$_{q=0}$ structure. However, unlike the V-AV$_{q=0}$ structure, the antivortex

4   generated through both cap and core switches remains stable along with the vortex without

5   their annihilations even they get very close. This behavior was also confirmed by

6   micromagnetic simulations (Figs. 3(b) and 3(c)). Figure 3(c) illustrates the detailed 3D

7   magnetic configurations of the V-AV$_{q=-1}$ structures at $H_x = 2$ mT and $H_x = 7$ mT marked by

8   the yellow dashed boxes in Fig. 3(b). The antivortex with $q_{AV} = -1/2$ moves toward the

9   vortex with $q_V = -1/2$ on the top surface of the rectangular element with increasing the field

10   to $H_x = 7$ mT. The antivortex structure and vortex structure are not annihilated even if they

11   get very close, and the V-AV$_{q=-1}$ structure on the top surface of the rectangular element

12   remains stable (green box in Fig.3(c)). By further micromagnetic simulations for the field-

13   driven behavior of the two structures performed in an identical rectangular element under the

14   magnetic field applied to the same direction, it was confirmed that the V-AV$_{q=0}$ structure is

15   indeed annihilated at $H_x = 4.3$ mT and $H_y = 10$ mT while the V-AV$_{q=-1}$ structure stays strong

16   without its annihilation even at high magnetic fields of $H_x = 8$ mT and $H_y = 14$ mT, which

17   quantitatively supports the higher stability of topologically non-trivial V-AV structure

18   (supplementary material: C). From the simulations, we also found that the overall field-driven

19   motions of the V-AV structures are the same regardless of the field direction. The magnetic

1   fields push the antivortex and the vortex structure toward each other, resulting in the

2   antivortex and the vortex becoming closer until they annihilate. However, when the magnetic

3   field is applied to the x-axis, the V-AV$_{q=0}$ structure is annihilated at a much lower field ($H_x =$

4   4.3 mT) than when the magnetic field is applied to the y-axis (H_y = 10 mT). The shape

5   anisotropy might make the V-AV structure more perturbed when the magnetic field is applied

6   in the x-axis. It is expected that the V-AV$_{q=0}$ structure is annihilated under the magnetic field

7   applied in the x-axis lower than H_x = 7 mT in experiments. The results in Fig. 3 support that

8   the annihilation of the topologically non-trivial V-AV structure does not occur easily, and

9   that the V-AV$_{q=-1}$ structure is more stable than the V-AV$_{q=0}$ structure. The higher stability of

10   the topologically non-trivial V-AV structure could be understood from topologically

11   perspective. The transformation of the V-AV$_{q=-1}$ structure into a topologically trivial structure

12   with q = 0 is difficult to happen because the topologically non-trivial V-AV structure must

13   overcome a high energy barrier dictated by topology to be converted into a topologically

14   trivial magnetic structure.

15   For a clearer interpretation of the higher stability of V-AV$_{q=-1}$ structure compared to

16   the V-AV$_{q=0}$ structure, we investigated the annihilation process of the V-AV$_{q=-1}$ structure by

17   applying higher magnetic field (Fig. 4). We observed that the annihilation of the V-AV$_{q=-1}$

18   structure happens at H_y = 19 mT (Figs. 4(a) and 4(b)). Interestingly, the annihilation of the V-

19   AV$_{q=-1}$ structure is achieved through the injection of a magnetic singularity called Bloch

1   point, the vanishing point of local magnetization ($m_x = m_y = m_z = 0$) (Fig. 4(a)).[37-42] The Bloch

2   point injection is revealed in the change of magnetic contrasts around the kinked area (Fig.

3   4(b)). The vertical boundary between upward and downward ABWs at $H_y = 18.9$ mT changes

4   to the diagonal boundary at $H_y = 19$ mT. A Bloch point is injected from the top surface of the

5   rectangular element where the V-AV$_{q=-1}$ structure is present (Fig. 4(c)). Simultaneously, V-

6   AV$_{q=-1}$ structure is annihilated. Then, the Bloch point is stabilized in the middle part of the

7   rectangular element. The results in Fig. 4 show that the annihilation of V-AV$_{q=-1}$ structure can

8   occur when a strong external perturbation such as a magnetic field enough to trigger the

9   injection of the Bloch point, is applied (supplementary material: D). The annihilation

10   mechanism of the topologically non-trivial V-AV structure involving Bloch point is clearly

11   distinguished from that of the topologically trivial V-AV structure.

12   In summary, we directly observe V-AV structures with different topologies stably

13   formed in Ni$_{80}$Fe$_{20}$ rectangular elements, where intriguing 3D magnetic structures with non-

14   uniform magnetization along the thickness direction are created, utilizing MTXM

15   measurements, and comprehensively understand their 3D magnetic configurations using

16   micromagnetic simulations. We find that the topologically trivial V-AV structure is easily

17   annihilated during its field-driven motion while the topologically non-trivial V-AV structure

18   stays stable without its annihilation. Our results show that the topologically non-trivial V-AV

19   structure has higher stability than the topologically trivial V-AV structure. We demonstrate

1   that the annihilation of the topologically non-trivial V-AV structure can be achieved only

2   through the injection of the Bloch point and this is responsible for the higher stability of

3   topologically non-trivial V-AV structure. This work provides fundamental scientific insight

4   into the stability of V-AV structures dictated by topology, which is also highly relevant to the

5   technological applications of topological magnetic structures.

1   SUPPLEMENTARY MATERIALS

2   See supplementary material for the details of MTXM measurements and

3 micromagnetic simulations, the detailed description to calculate the topological charge of V-

4 AV structures, the additional micromagnetic simulation results for the stability of V-AV

5 structures with different topologies, and the discussion of the stability of V-AV structures in

6 the topological and energetic perspective.

ACKNOWLEDGEMENT

1 **DATA AVAILABILITY**

2   The data that support the findings of this study are available from the corresponding

3 author upon reasonable request.

REFERENCES

1. Naoto Nagaosa and Yoshinori Tokura, Nature Nanotechnology **8** (12), 899 (2013).

2. Wanjun Jiang, Xichao Zhang, Guoqiang Yu, Wei Zhang, Xiao Wang, M. Benjamin Jungfleisch, John E Pearson, Xuemei Cheng, Olle Heinonen, Kang L. Wang, Yan Zhou, Axel Hoffmann, and Suzanne G E te Velthuis, Nature Physics **13** (2), 162 (2017).

3. Russell P. Cowburn, Nature Materials **6** (4), 255 (2007).

4. Mi-Young Im, Peter Fischer, Keisuke Yamada, Tomonori Sato, Shinya Kasai, Yoshinobu Nakatani, and Teruo Ono, Nature Communications **3** (1), 983 (2012).

5 Seonghoon Woo, Kyung Mee Song, Hee-Sung Han, Min-Seung Jung, Mi-Young Im, Ki-Suk Lee, Kun Soo Song, Peter Fischer, Jung-Il Hong, Jun Woo Choi, Byoung-Chul Min, Hyun Cheol Koo, and Joonyeon Chang, Nature Communications **8** (1), 15573 (2017).

6. Hans-Benjamin Braun, Advances in Physics **61** (1), 1 (2012).

7. Soong-Geun Je, Hee-Sung Han, Se Kwon Kim, Sergio A. Montoya, Weilun Chao, Ik-Sun Hong, Eric E. Fullerton, Ki-Suk Lee, Kyung-Jin Lee, Mi-Young Im, and Jung-Il Hong, ACS Nano **14** (3), 3251 (2020).

8. Junwei Zhang, Xiaomin Zhang, Huanjian Chen, Yao Guang, Xue Zeng, Guoqiang Yu, Senfu Zhang, Yizhou Liu, Jiafeng Feng, Yuelei Zhao, Yan Zhou, Xuepeng Qiu, Xiufeng Han, Yong Peng, and Xixiang Zhang, Applied Physics Letters **116** (14), 142404 (2020).

9. K. Shigeto, T. Okuno, K. Mibu, T. Shinjo, and T. Ono, Applied Physics Letters **80** (22), 4190 (2002).

10. N. Gao, S. G. Je, M. Y. Im, J. W. Choi, M. Yang, Q. Li, T. Y. Wang, S. Lee, H. S. Han, K. S. Lee, W. Chao, C. Hwang, J. Li, and Z. Q. Qiu, Nature Communications **10** (1), 5603 (2019).

11. P. E. Roy, J. H. Lee, T. Trypiniotis, D. Anderson, G. A. C. Jones, D. Tse, and C. H. W. Barnes, Physical Review B **79** (6), 060407 (2009).

12. Mi-Young Im, Peter Fischer, Hee-Sung Han, Andreas Vogel, Min-Seung Jung, Weilun Chao, Young-Sang Yu, Guido Meier, Jung-Il Hong, and Ki-Suk Lee, NPG Asia Materials **9** (2), e348 (2017).

13. J. Li, A. Tan, K. W. Moon, A. Doran, M. A. Marcus, A. T. Young, E. Arenholz, S. Ma, R. F. Yang, C. Hwang, and Z. Q. Qiu, Applied Physics Letters **104** (26), 262409 (2014).

14. Ki-Suk Lee, Byoung-Woo Kang, Young-Sang Yu, and Sang-Koog Kim, Applied Physics Letters **85** (9), 1568 (2004).

15. R. Hertel, S. Gliga, M. Fähnle, and C. M. Schneider, Physical Review Letters **98** (11), 117201 (2007).

16. Riccardo Hertel and Claus M. Schneider, Physical Review Letters **97** (17), 177202 (2006).

17. Oleg Tchernyshyov and Gia-Wei Chern, Physical Review Letters **95** (19), 197204 (2005).

18. N. D. Mermin, Reviews of Modern Physics **51** (3), 591 (1979).

19. O. A. Tretiakov and O. Tchernyshyov, Physical Review B **75** (1), 012408 (2007).

20. Wataru Koshibae and Naoto Nagaosa, preprint arXiv: 2005.04516v1 (2020).

21. Matthias Noske, Hermann Stoll, Manfred Fähnle, Riccardo Hertel, and Gisela Schütz, Physical Review B **91** (1), 014414 (2015).

22. Ki-Suk Lee, SangKook Choi, and Sang-Koog Kim, Applied Physics Letters **87** (19), 192502 (2005).

23. Sri Sai Phani Kanth Arekapudi, Benny Böhm, Lakshmi Ramasubramanian, Fabian Ganss, Peter Heinig, Sven Stienen, Ciarán Fowley, Kilian Lenz, Alina M. Deac, Manfred Albrecht, and Olav Hellwig, Physical Review B **103** (1), 014405 (2021).

24. Kyoung-Woong Moon, Jungbum Yoon, Changsoo Kim, and Chanyong Hwang, Physical Review Applied **12** (6), 064054 (2019).

25. Shilei Zhang, Alexander A. Baker, Stavros Komineas, and Thorsten Hesjedal, Scientific Reports **5** (1), 15773 (2015).

26. J. Hagemeister, N. Romming, K. von Bergmann, E. Y. Vedmedenko, and R. Wiesendanger, Nature Communications **6** (1), 8455 (2015).

27. Hiroshi Oike, Akiko Kikkawa, Naoya Kanazawa, Yasujiro Taguchi, Masashi Kawasaki, Yoshinori Tokura, and Fumitaka Kagawa, Nature Physics **12** (1), 62 (2016).

28. David Cortés-Ortuño, Weiwei Wang, Marijan Beg, Ryan A. Pepper, Marc-Antonio Bisotti, Rebecca Carey, Mark Vousden, Thomas Kluyver, Ondrej Hovorka, and Hans Fangohr, Scientific Reports **7** (1), 4060 (2017).

29. Arne Vansteenkiste, Jonathan Leliaert, Mykola Dvornik, Mathias Helsen, Felipe Garcia-Sanchez, and Bartel Van Waeyenberge, AIP Advances **4** (10), 107133 (2014).

30. L. Landau and E. Lifshitz, Phys. Z. Sowjetunion **8**, 153–164 (1935); see also L. Landau and E. Lifshitz, in *Perspectives in Theoretical Physics*, edited by L. P. Pitaevski (Pergamon, Amsterdam, 1992), pp. 51.

31. T. L. Gilbert, Phys. Rev. **100**, 1243 (1955).

32. F. Cheynis, A. Masseboeuf, O. Fruchart, N. Rougemaille, J. C. Toussaint, R. Belkhou, P. Bayle-Guillemaud, and A. Marty, Physical Review Letters **102** (10), 107201 (2009).

33. A. Masseboeuf, O. Fruchart, J. C. Toussaint, E. Kritsikis, L. Buda-Prejbeanu, F. Cheynis, P. Bayle-Guillemaud, and A. Marty, Physical Review Letters **104** (12), 127204 (2010).

34. A. Hubert and R. Schäfer, *Magnetic Domains: The Analysis of Magnetic Microstructures*. (Springer, 1998).

35. Riccardo Hertel and Helmut Kronmüller, Physical Review B **60** (10), 7366 (1999).

36. Hee-Sung Han, Sooseok Lee, Dae-Han Jung, Myeonghwan Kang, and Ki-Suk Lee, Applied Physics Letters **117** (4), 042401 (2020).

37. Mi-Young Im, Hee-Sung Han, Min-Seung Jung, Young-Sang Yu, Sooseok Lee, Seongsoo Yoon, Weilun Chao, Peter Fischer, Jung-Il Hong, and Ki-Suk Lee, Nature Communications **10** (1), 593 (2019).

38. Ernst Feldtkeller, IEEE Transactions on Magnetics **53** (10), 1 (2017).

39. W. Döring, Journal of Applied Physics **39** (2), 1006 (1968).

40. C. Donnelly, M. Guizar-Sicairos, V. Scagnoli, S. Gliga, M. Holler, J. Raabe, and L. J. Heyderman, Nature **547** (7663), 328 (2017).

41. Claire Donnelly, Konstantin L. Metlov, Valerio Scagnoli, Manuel Guizar-Sicairos, Mirko Holler, Nicholas S. Bingham, Jörg Raabe, Laura J. Heyderman, Nigel R. Cooper, and Sebastian Gliga, Nature Physics **17** (3), 316 (2021).

42. A. Hierro-Rodriguez, C. Quirós, A. Sorrentino, L. M. Alvarez-Prado, J. I. Martín, J. M. Alameda, S. McVitie, E. Pereiro, M. Vélez, and S. Ferrer, Nature Communications **11** (1), 6382 (2020).

FIGURE CAPTIONS

2 FIG. 1. (a) Schematic diagram of magnetic imaging utilizing magnetic transmission soft X-

3 ray microscopy (MTXM). (b)-(g) Out-of-plane magnetic structures in various $Ni_{80}Fe_{20}$

4 rectangular-patterned elements observed by (b)-(d) MTXM measurements and (e)-(g)

5 micromagnetic simulations with consideration of magnetic grains. The black and white

6 contrasts in (b)-(g) indicate the upward and downward out-of-plane (OOP) magnetic

7 components, respectively. The zoomed images for detailed magnetic configurations near the

8 kinked area of domain walls are inserted. The red and blue dotted lines represent domain wall

9 segments with upward and downward magnetizations, respectively. (h)-(j) Three-dimensional

10 illustrations of magnetic structures in the yellow dotted boxes of (b)-(g). The red and blue

11 colors represent volumes with the normalized magnetizations of with $m_z \geq +0.8$ and $m_z \leq$

12 -0.8, respectively. The black streamlines with arrows indicate the direction of the in-plane

13 magnetization. The cross-section images of magnetic configurations on the plane at the center

14 of element ($x = 0$) in (h) and on the planes at $x = -120$ nm and $x = +120$ nm in (i) and (j) are

15 added.

16

17 FIG. 2. Field-driven motion of the V-AV$_{q=0}$ structure observed by (a) MTXM measurements

18 and (b) micromagnetic simulations with consideration of magnetic grains. The magnetic field

19 was applied in y-axis. The black and white contrasts indicate the upward and downward

20 magnetic components, respectively. In (a) and (b), the vortex and antivortex constituting the

21 vortex-antivortex structure together are indicated by V and AV, respectively. (c) The

22 annihilation process of V-AV$_{q=0}$ structure (yellow dotted boxes in (b)) and the internal

1 magnetic configuration of the structure during the process are illustrated. q_V, q_{AV} and q_{V-AV}

2 indicate q of the vortex, antivortex, and V-AV$_{q=0}$ structure, respectively.

3

4

5 FIG. 3. Field-driven motion of the V-AV$_{q=-1}$ structure observed by (a) MTXM measurements

6 and (b) micromagnetic simulations with consideration of magnetic grains. The magnetic field

7 was applied in x-axis. The black and white contrasts indicate the upward and downward

8 magnetic components, respectively. (c) The internal magnetic configurations of the vortex

9 and antivortex structures at H_x = 2 mT and H_x = 7 mT are illustrated. q_V, q_{AV} and q_{V-AV}

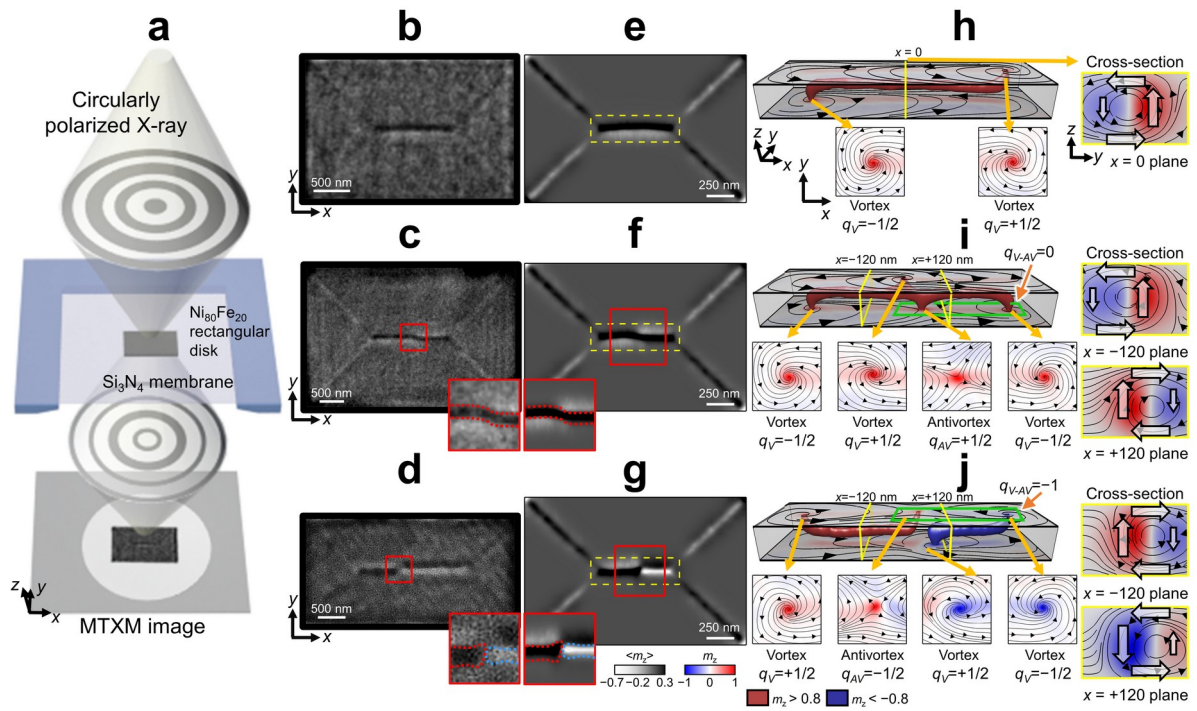10 indicate q of the vortex, antivortex, and V-AV structure, respectively.

11

12

13 FIG. 4. (a) Three-dimensional illustration of the annihilation of the V-AV$_{q=-1}$ structure by

14 applying the magnetic field in y-axis, and (b) their out-of-plane magnetic structure where the

15 black and white contrasts indicate upward and downward magnetic components, respectively.

16 q_{V-AV} indicates the q of the V-AV structure. (c) The annihilation process of the V-AV$_{q=-1}$

17 structure by the injection of the Bloch point. The green sphere in (a) and (c), represents the

18 Bloch point. Transparency indicates sequential order of the V-AV$_{q=-1}$ annihilation.
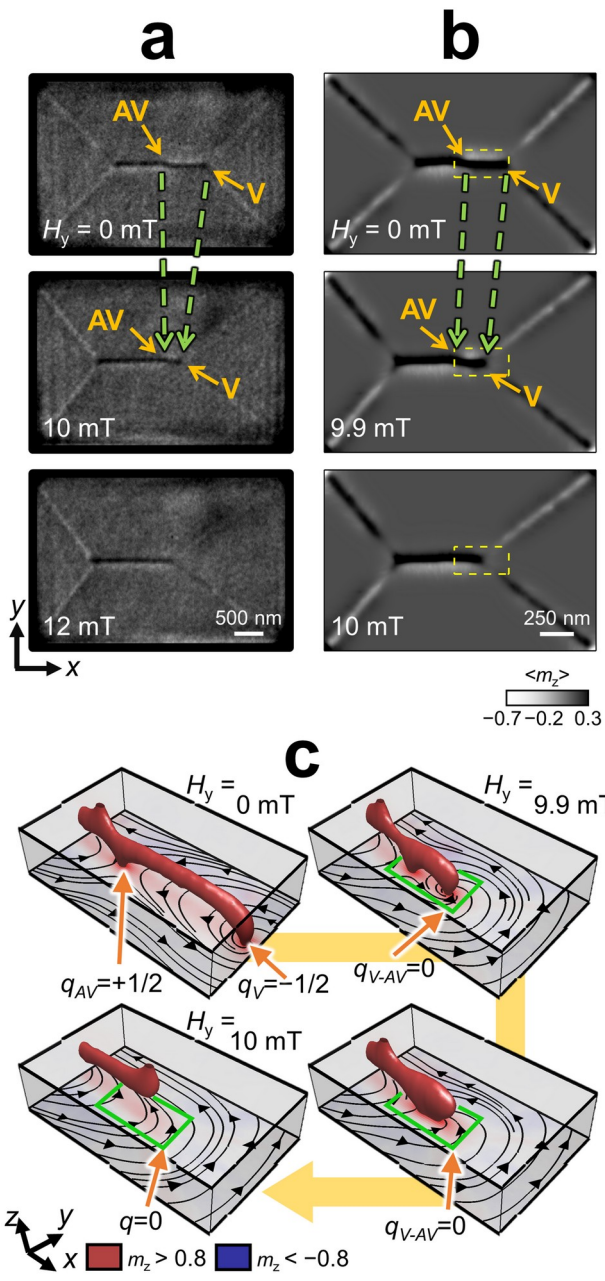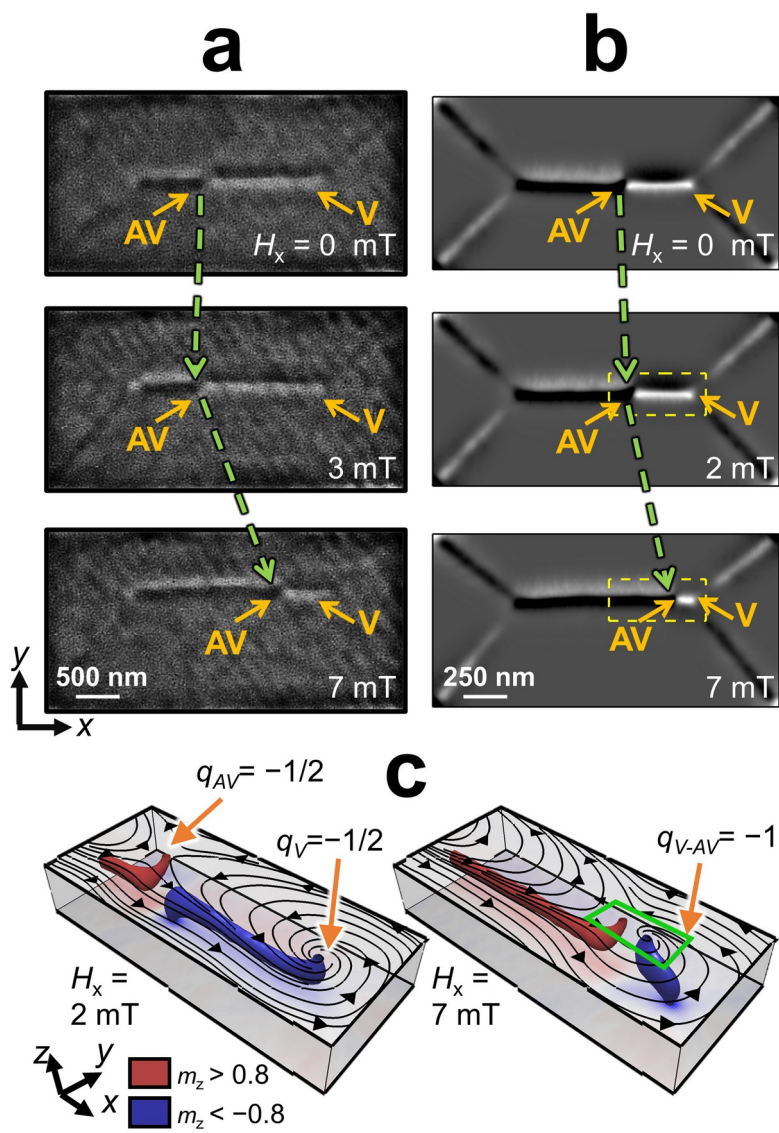
19

FIGURE

FIGURE 1

a

AV

V

H_y = 0 mT

AV

V

10 mT

12 mT

500 nm

y

x

b

AV

V

H_y = 0 mT

AV

V

9.9 mT

10 mT

250 nm

$<m_z>$

−0.7 −0.2 0.3

c

H_y = 0 mT

q_{AV}=+1/2 q_V=−1/2

H_y = 9.9 mT

q_{V-AV}=0

H_y = 10 mT

q=0

q_{V-AV}=0

z

y

x m_z > 0.8 m_z < −0.8

1

2   FIGURE 2

3

FIGURE 3

FIGURE 4